Universal Design Platform for an Extended Class of Photonic Dirac Cones

Jungmin Kim, Sunkyu Yu,* and Namkyoo Park†
Photonic Systems Laboratory, Department of Electrical and Computer Engineering, Seoul National University, Seoul 08826, Republic of Korea

(Received 24 October 2019; revised manuscript received 7 February 2020; accepted 18 March 2020; published 7 April 2020)

Band engineering near Dirac points is an emerging topic in condensed matter physics and photonics, enabling multifaceted devices of record-high conductivity and zero refractive index in both electronic and photonic structures. Recently, an extended class of Dirac cone, type I, II, or III, has attracted much attention with its controlled directionality of singular wave behaviors near the Dirac points. However, despite the significance of the discovery and applications of each type of Dirac cone, the theoretical framework and unified design structure bridging different types of Dirac cones have not been clearly elucidated. Here, we propose a universal design platform for all types of photonic Dirac cones and reveal the key parameter determining their types and transformations. Starting from the accidentally induced photonic Dirac cone, we show that the inverse design of an optical potential landscape enables the deterministic control of the spectral ordering, which leads to designer construction of each type of Dirac cone. This approach will pave the way for the design of artificial degeneracies with tunable anisotropy for general wave systems.

DOI: 10.1103/PhysRevApplied.13.044015

I. INTRODUCTION

A Dirac cone, a conical dispersion with point degeneracy (Dirac point; DP), has been a focus of research in condensed matter physics with its unique property of massless transport of electrons [1]. This novel feature, originating from the sublattice symmetry in a honeycomb lattice, has led to significant advances in high-performance graphene electronics [2,3] and spintronics [4,5]. Because of the universality of band theory in wave phenomena, the physics and applications of DPs have also been widely reproduced in other wave systems, including photonic [6–9], phononic [10,11], and circuit [12,13] structures. In particular, the photonic Dirac cone (PDC), accidentally induced at the Γ-point with an additional flat band, became a representative optical counterpart of massless electronic transport, achieving amplitude-phase-conserved wave propagation with a zero refractive index. The Dirac frequency in the PDC then operates as an electromagnetic resonant frequency where the effective electric and magnetic dipole moments simultaneously cancel external fields, defining the phase transition for optical materials between negative and positive refractive indices [7,8].

The physics and its applications near DPs have been further extended by imposing a perturbation on the perfect conical band structure [Fig. 1(a)], which derives significant phase change around the DP. For example, in quantum mechanics, a band-gap opening realized by broken time-reversal symmetry with an external magnetic field gives rise to nonzero Chern numbers and topological edge states [14]. Similar band manipulations by artificial gauge fields have also been reported with the emergence of nontrivial spin Chern numbers and the analogy of the quantum spin Hall effect in classical wave systems: photonics [15,16], acoustics [17,18], and electric circuit systems [12,13]. Different classes of *tilted* Dirac cones have also attracted much recent interest with their anisotropic Fermi surfaces. In terms of the band slopes near DPs, Dirac cones are classified by type I, II, or III, each having opposite signs, the same signs, or a zero of group velocities [Figs. 1(b)–1(d)], resulting in different anisotropic Fermi surfaces (or isofrequency contours; IFCs) at the Dirac frequency [19,20]. While tilted type-I and type-III (as an extreme case of type-I) DPs are realized by imposing smooth deformations on structures in both quantum systems [21,22] and photonics [20,23,24], it is only recently that type-II Dirac-Weyl points with extreme nonreciprocity have attracted attention [19,25], reproduced in photonics [26–29] and acoustics [30–32]. While each type of tilted Dirac cone in given structures has been well elucidated in terms of its mechanisms and behavior and is also considered a promising platform for imposing directionality on Dirac cones, the study of the relationships between different type of DPs in terms of physics and platform compatibility is rare.

In this paper, we present an integrated analysis for all types of tilted PDCs and thus achieve a universal design framework to enable the deterministic realization of and transition between different types of tilted Dirac cones.

*skyu.photon@gmail.com
†nkpark@snu.ac.kr

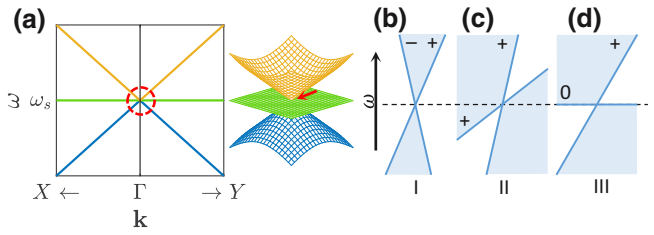

FIG. 1. (a) Band dispersion of a photonic Dirac cone with accidental triple degeneracy $\omega_s = \omega_{px} = \omega_{py}$ along the ΓX and ΓY paths. ω_s and $\omega_{px,py}$ are the eigenfrequencies of a monopole and dipoles at the Γ-point, and Γ, $X(Y)$ are the reciprocal points in the square Brillouin zone. (b)–(d) Schematics of vertical cross sections for tilted PDCs: (b) type I, (c) type II, and (d) type III.

Starting from the effective Hamiltonian theory, we first classify deformed band structures of the accidental PDC [7] in terms of the spectral ordering of eigenvalues at the Γ-point. We then propose a perturbative inverse-design method that utilizes the spatial profile of a *target* eigenmode, achieving the successful generation of deformed dispersions that cover all types of tilted PDCs. Under the same template, we also study and reveal the frequency-dependent topological transition of IFCs in the momentum space. The effect of mirror symmetry breaking is also discussed in regard to the opening of the symmetry-protected band gap.

II. EFFECTIVE HAMILTONIAN DESCRIPTION

Without loss of generality, we consider a two-dimensional square-lattice photonic crystal consisting of isotropic and nonmagnetic materials for transverse-magnetic propagations. In these platforms, the application of the $k \cdot p$ perturbation theory allows the approximation of band structures in the vicinity of the Γ-point, using eigenmodes and corresponding eigenfrequencies at the Γ-point [33]. For nearly degenerate dipole modes $|p_{x,y}\rangle$ and monopole mode $|s\rangle$, the effective Hamiltonian for the eigenvalue equation $H(\mathbf{k})\,|u_\mathbf{k}\rangle = \omega(\mathbf{k})\,|u_\mathbf{k}\rangle$ then becomes

$$H(\mathbf{k}) = \begin{bmatrix} \omega_s & v_x k_x & v_y k_y \\ v_x k_x & \omega_{px} & 0 \\ v_y k_y & 0 & \omega_{py} \end{bmatrix}, \tag{1}$$

where the diagonal terms (ω_s and $\omega_{px,py}$) are the unperturbed eigenfrequencies of a monopole and x and y dipoles at the Γ-point, respectively, satisfying $H(0)\,|s\rangle = \omega_s\,|s\rangle$ and $H(0)\,|p_{x,y}\rangle = \omega_{px,py}\,|p_{x,y}\rangle$. The off-diagonal terms ($v_x k_x$ and $v_y k_y$) are $\mathbf{k}$-dependent perturbations to the Γ-point Hamiltonian with group velocity coefficients $v_{x,y}$ [34]. For other lattice structures such as hexagonal [16] and rhombic [35] lattices, a similar formulation using their eigenmodes can be developed in a similar way.

For simplicity, we focus on the band structures along the k_x axis ($k_y = 0$). Along this axis, Hamiltonian H is decomposed into a 1×1 scalar operator for the p_y mode and a 2×2 Hamiltonian matrix for the coupled s and p_x modes. Three bands of the Hamiltonian are then obtained as a decoupled flat band $\omega_{\text{flat}}(k_x; k_y = 0) = \omega_{py}$ and the other coupled bands:

$$\omega_\pm(k_x; k_y = 0) = \frac{\omega_s + \omega_{px} \pm \sqrt{(\omega_s - \omega_{px})^2 + 4v_x^2 k_x^2}}{2} \tag{2}$$

with corresponding eigenmodes $|\text{flat}\rangle = |p_y\rangle$ and $|\pm\rangle = c_s^{(\pm)}\,|s\rangle + c_{px}^{(\pm)}\,|p_x\rangle$ for some normalized coefficients $c_s^{(\pm)}$ and $c_{px}^{(\pm)}$. We note that the geometry of the coupled bands $\omega_\pm$ near the Γ-point is mainly determined by the "diagonal" components ω_s and $\omega_{px,py}$ of the Hamiltonian.

According to Eq. (2), we note that three-level band structures of PDCs can be generally classified into the following five regimes, with respect to Γ-point spectral distributions: (A) $\omega_{px} = \omega_{py} = \omega_s$ [Fig. 1(a)], (B) $\omega_{px} = \omega_{py} < \omega_s$ [Fig. 2(a)], (C) $\omega_{py} < \omega_{px} < \omega_s$ [Fig. 2(b)], (D) $\omega_{py} < \omega_{px} = \omega_s$ [Fig. 2(c)], and (E) $\omega_{py} < \omega_s < \omega_{px}$ [Fig. 2(d)]. In terms of this spectral ordering, it now becomes easier and clearer to classify different types of PDC. First, class A, known as the accidental degeneracy [7,8], corresponds to the type-I PDC with an additional flat band [green band in Fig. 1(a)]. Classes B–E correspond to the deformed dispersion of the accidental PDC (class A). Typical C_{4v}-symmetric photonic crystals exemplify case B with parabolic dispersions due to nonzero $\omega_{px,py} - \omega_s$ [Fig. 2(a)] [36], while case D signifies the directional Dirac dispersion at the Γ-point [37]. In view of the inverse-design approach of the PDC, which will be expanded in Sec. III, it is worth mentioning that the Γ-point eigenfrequencies $\omega_{px,py}$ and ω_s strongly affect the effective electric and magnetic responses of materials and the detailed band geometry [37,38]. Also see Note S1 within the Supplemental Material [39].

Classifying the various dispersions of deformed PDC structures with the single Hamiltonian formulation, we search for the variations of tilted PDCs. For anisotropic classes C–E with broken C_{4v} symmetry, type-III PDCs can be achieved away from the Γ-point [black circles and arrows in Figs. 2(b)–2(d)]. As an example, we consider the emergence of a type-III PDC in class D of $\Delta\omega_{py} = \omega_{py} - \omega_s < 0$ [Fig. 2(c)], away from the Γ-point. For this case, since the band dispersions are given by $\omega_{\text{flat}}(k_x; k_y = 0) = \omega_{py}$ and $\omega_\pm(k_x; k_y = 0) = \omega_s \pm |v_x k_x|$ from Eq. (2), there exists a single intersecting point between $\omega_-(k_x; k_y = 0)$ and $\omega_{\text{flat}}(k_x; k_y = 0)$ bands at $k_x = k_{x0} \equiv |\Delta\omega_{py}/v_x|$. In contrast, a nonzero k_y in the effective Hamiltonian leads to anticrossing between two bands with the frequency splitting $|\omega_- - \omega_{\text{flat}}| \sim \sqrt{2} v_y k_y$ with mode coupling [Fig. 2(e); also refer to Appendix A for the derivation]. The crossing and anticrossing depending on k_y prove that there is

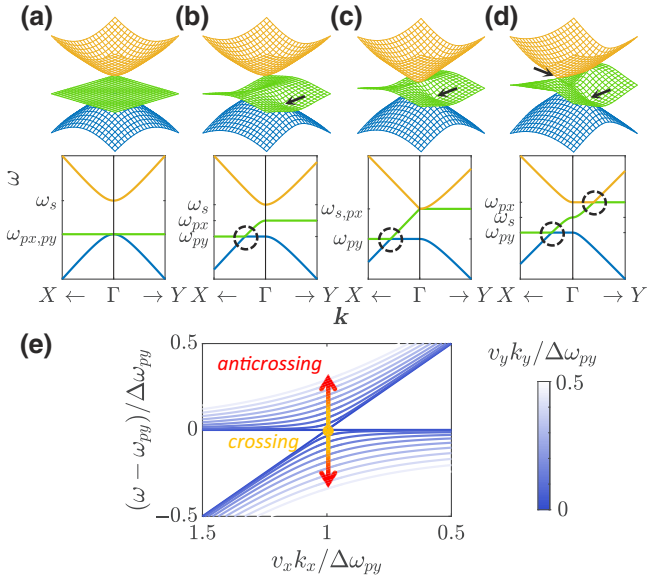

FIG. 2. (a)–(d) Deformed band structures with Γ-point spectral distributions $\omega_{px} = \omega_{py} < \omega_s$, $\omega_{py} < \omega_{px} < \omega_s$, $\omega_{py} < \omega_{px} = \omega_s$, and $\omega_{py} < \omega_s < \omega_{px}$, respectively. The dotted circles and arrows in (b)–(d) indicate the emergence of type-III PDCs through anisotropic deformations. (e) Projections of band structures on the normalized k_x-ω plane, near the type-III PDC in (c), describing the band crossing and anticrossing depending on the values of k_y. The graded color of lines represents the values of normalized k_y.

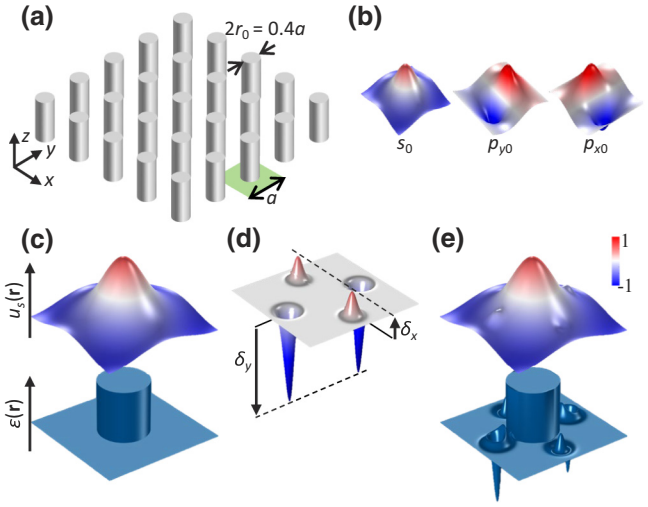

FIG. 3. (a) Dielectric rod structure on a square lattice (radius $r_0 = a/5$, dielectric constant $\epsilon = 12.5$) [7] as a seed potential for class A in Fig. 1(a). (b) Three eigenmode profiles (one monopole s_0 and two dipoles $p_{x0,y0}$) at the Γ-point for the potential in (a), with degenerate eigenfrequency $\omega a/2\pi c = 0.541$. (c)–(e) Inverse design schematics. (c) The unperturbed PDC potential $\epsilon_0(\mathbf{r})$ (lower) and its s-mode profile (upper). (d) The C_{2v}-symmetric perturbation function $f(\mathbf{r})$ with control parameters δ_x and δ_y. (e) A new target s-mode profile (upper) and the inversely designed potential with the fixed eigenfrequency $\omega_s = \omega_{s0}$ (lower). The target mode is defined by multiplying the perturbation function $f(\mathbf{r})$ with the unperturbed s-mode profile.

a *point* degeneracy at $\mathbf{k} = (k_{x0}, 0)$ for the formation of a PDC. Because of the zero group velocity $\partial\omega_{\text{flat}}/\partial k_x = 0$, the band structures near this band-crossing point are classified as type III, which is also discussed in a similar way in Ref. [20]. We further note for later discussions that the bending of the flat band $\omega_{\text{flat}}(k_x)$ also allows the transition of type-III PDCs to type-I or type-II PDCs. Most importantly, we show that this transition between different types of the PDCs can be controlled by the spectral separation $\Delta\omega_{px,py} \equiv \omega_{px,py} - \omega_s$.

III. INVERSE DESIGN OF TILTED DIRAC CONES

To achieve the optical potential for the target Hamiltonian in Eq. (1), we apply the inverse molding of the potential landscape from the spatial profile of an eigenmode, which has been adopted in the design of disordered structures [40], non-Hermitian potentials [41], and the transverse spin of light [42]. For the Helmholtz equation $[\nabla^2 + k_0^2\epsilon(\mathbf{r})]E_z(\mathbf{r}) = 0$, the target profile of the Bloch wave $E_z(\mathbf{r}) = e^{i\mathbf{k}\cdot\mathbf{r}}u_{\mathbf{k}}(\mathbf{r})$ at the design point $(\mathbf{k}, \omega)$ provides a necessary landscape of permittivity in a unit cell:

$$\epsilon(\mathbf{r}) = \frac{(k^2 - \nabla^2)u_{\mathbf{k}} - 2i\mathbf{k}\cdot\nabla u_{\mathbf{k}}}{k_0^2 u_{\mathbf{k}}}, \tag{3}$$

where $k = |\mathbf{k}|$, $k_0 = \omega/c$, and the modal profile inside the unit cell $u_{\mathbf{k}}(\mathbf{r})$ has the same periodicity as $\epsilon(\mathbf{r})$. For the three eigenmodes [Fig. 3(b)], the inverse design process allows the designer alteration of the two $p_{x,y}$ eigenmodes and their eigenfrequencies using the spatial profile of target s mode $u_s(\mathbf{r}) = \langle\mathbf{r}|s\rangle$.

In detail, we introduce a C_{2v}-symmetric perturbation $f(\mathbf{r})$ [Fig. 3(d)] to the s mode of the potential [Fig. 3(c)] for class A [Fig. 1(a)]. This wave function perturbation on a target eigenmode $|s\rangle = \exp[f(\mathbf{r})]\,|s_0\rangle$ [Fig. 3(e), upper] then leads to the designed potential landscape $\epsilon(\mathbf{r})$ [Fig. 3(e), lower], with Eq. (3) at fixed momentum and frequency $(\mathbf{k}, \omega) = (0, \omega_{s0})$. We emphasize that the inverse-designed potential from this C_{2v}-symmetric perturbation maintains the original C_{2v} symmetry while keeping the orthogonality between the bases of the Hamiltonian in Eq. (1). Critically, their mode frequencies are adjusted by the modified effective index for each mode, in such a way to derive the *nonzero* dipole resonance shifts $\Delta\omega_{px,py} \neq 0$ and the *zero* monopole mode resonance shift $\Delta\omega_s = 0$, thereby breaking the accidental degeneracy. To achieve the target $\Delta\omega_{px,py}$, we utilize parameters (δ_x, δ_y) that separately determine the strength of the perturbation $f(\mathbf{r})$ in each axis, as described in Appendix B with detailed numerical treatment. See also Note S2 within the Supplemental

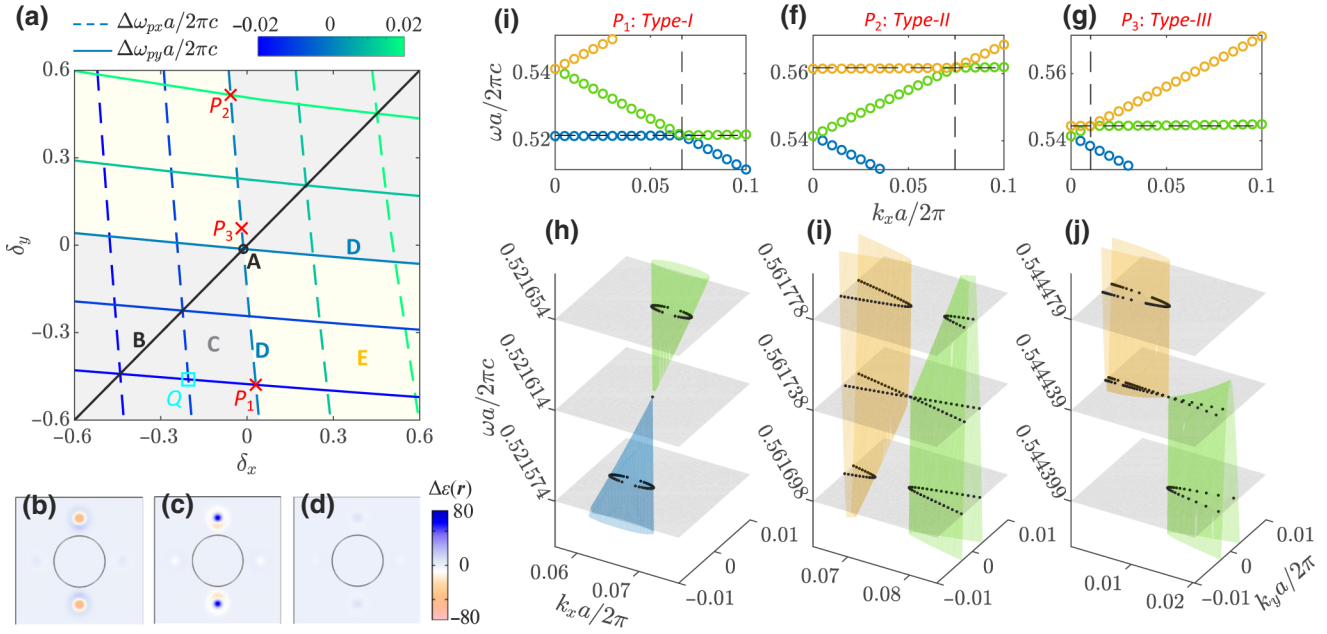

FIG. 4. Inverse design of the deformed structures using parameters (δ_x, δ_y). (a) Contour lines of the modal separations $\Delta\omega_{px,py}$ as a function of (δ_x, δ_y). The phase diagram in (δ_x, δ_y) space represents the deformation classes A–E. Representative design points $P_1 = (0.03, -0.48)$, $P_2 = (-0.06, 0.52)$, and $P_3 = (-0.02, 0.06)$ correspond to the type-I-, type-II-, and type-III-like DPs. Design point $Q = (-0.20, -0.46)$ corresponds to another DP in relation to mirror symmetry breaking in Sec. IV. (b)–(d) Potential differences $\Delta\epsilon(\mathbf{r}) = \epsilon(\mathbf{r}) - \epsilon_0(\mathbf{r})$ inversely designed from $P_{1,2,3}$, respectively. Circles indicate the size and the position of the seed rods. (e)–(g) Band dispersions along the k_x axis of photonic crystals corresponding to $P_{1,2,3}$. (h)–(j) Band dispersions near the DPs with IFCs (black dots) around the Dirac frequencies for $P_{1,2,3}$, respectively.

Material [39] for a dipole-based design approach, where the perturbation is applied to the p_x mode.

To verify the proposed idea, the dipole frequency shifts $\Delta\omega_{px,py}$ are calculated with the finite element method (FEM) [43] as a function of (δ_x, δ_y). The contours of modal separations $\Delta\omega_{px}$ (dashed lines) and $\Delta\omega_{py}$ (solid lines) in Fig. 4(a) are almost perpendicular to the δ_x and δ_y axes, respectively, proving the nearly independent control of ω_{px} and ω_{py} with respect to the fixed ω_s. We emphasize that all five classes discussed in Figs. 1 and 2 are classified as different regimes in the (δ_x, δ_y) plane [Fig. 4(a): $\Delta\omega_{px} = \Delta\omega_{py} = 0$, point A; $\Delta\omega_{px} = \Delta\omega_{py}$, line B; $\Delta\omega_{px}\Delta\omega_{py} = 0$, lines D; gray and yellow regions C, E], proving the emergence of entire classes of the deformed structures within a single platform.

Because the flat band has a nonzero curvature in a real structure, especially for large k values, other types of PDC having a positive or negative slope are expected to emerge, as derivatives of type III. For precise analysis beyond the $k \cdot p$ effective Hamiltonian for large k, we use the FEM in the analysis of the dispersions. The result of the FEM analysis produces a small but positive group velocity $0 < \partial\omega_{\text{flat}}/\partial k_x \ll |v_x|$ as expected, providing an additional degree of freedom for the design of tilted PDCs. For instance, we consider three cases $P_{1,2,3}$ of deformation, class D in Fig. 4(a), having $\Delta\omega_{py}a/2\pi c = +0.02, -0.02,$ and $+0.003$ [Figs. 4(e)–4(g)], respectively, while preserving $\Delta\omega_{px} = 0$. As shown in Figs. 4(e)–4(g), the dispersion and type of the PDC are then controlled by $\Delta\omega_{py}$, which determines the relative position of the flatlike band frequency: below, above, or near the frequency $\omega_s = \omega_{px} \sim 0.541 \times 2\pi c/a$ for points $P_{1,2,3}$, respectively. The flat band for each point then intersects with different dispersion bands having opposite slope $\omega_{\pm}(k_x) \approx \omega_s \pm |v_x k_x|$: P_1 for ω_+ and $P_{2,3}$ for ω_-. Further, it is noted that these spectral relations follow the general classification of the tilted PDCs: type I [$\partial\omega_{\text{flat}}/\partial k_x > 0$, $\partial\omega_-/\partial k_x < 0$, Fig. 1(b)] for P_1, type II [$\partial\omega_{\text{flat}}/\partial k_x > 0$, $\partial\omega_+/\partial k_x > 0$, Fig. 1(c)] for P_2, and type III [$\partial\omega_{\text{flat}}/\partial k_x \sim 0$, $\partial\omega_+/\partial k_x > 0$, Fig. 1(d)] for P_3. Further discussions on the control of the group velocity $\partial\omega_{\text{flat}}/\partial k_x$ [44] are given in Note S3 within the Supplemental Material [39].

Furthermore, each type of achieved PDC leads to the different classes of the topological transition in k space [42,45,46] around the DPs: elliptic-to-elliptic [Fig. 4(h)], hyperbolic-to-hyperbolic [Fig. 4(i)], and asymmetric hyperbolic-to-hyperbolic [Fig. 4(j)] transitions, respectively, for types I–III. Thus, the successful design of all types of PDCs in a single platform and the subsequent tunable topological transition in the momentum space are proved, importantly, in addition to significantly distinct IFCs at the Dirac frequency (single-point, two-line, and asymptotically single-line IFCs in types

I–III, respectively). We emphasize that the distinctive IFC of each Dirac cone is determined by the separation of participating states [yellow, green, or blue colors in Figs. 4(e)–4(g)]; type I and II each shows the ω-domain and k-domain separation of states, respectively, while type III presents the simultaneous separation in both k and ω domains. Near these distinctive IFCs, a significantly different momentum distribution around the original DP can be achieved even with the small frequency shift of the flat band. Although the observed transition corresponds to the small-signal momentum perturbation around the Dirac momentum state, when the time-reversal symmetry is broken and thus a similar transition can occur at the Γ-point DP, the abrupt material phase transition with positive (elliptic) to negative (hyperbolic) refraction can also be realized with broken reciprocity.

IV. BAND-GAP OPENING IN TILTED PDCs

Band-gap opening at the DPs arises from the introduction of symmetry breaking, which leads to anticrossing of the degenerate bands, such as the inversion symmetry in a honeycomb lattice [47,48] or a square lattice [24]. The transition from Dirac cones with linear dispersions to band gaps with parabolic dispersions has enabled various practical applications in graphene switching devices [49] and tuning of Purcell factors [50]. In the proposed universal platform, we investigate the realization of a band-gap opening in tilted PDCs by breaking the mirror symmetry of C_{2v}. We impose the following modification: $\delta_{x,y}(1 \pm \rho_{x,y})$ on the original perturbation for the type-III PDC [Fig. 5(b)] to obtain new mirror-symmetry-broken perturbations [Figs. 5(a) and 5(c)], where $\rho_{x,y}$ allows the mirror-asymmetric potential in the unit cell. Due to the inherent anisotropy of the tilted PDC, the response of the PDC to the mirror-symmetry-broken modification is different for each case of $\rho_x \neq 0$ and $\rho_y \neq 0$. First, for $|\text{flat}\rangle = |p_y\rangle$ and $|\pm\rangle = c_s|s\rangle + c_{px}|p_x\rangle$ with arbitrary coefficients c_s and c_{px}, the y-directional symmetry breaking ($\rho_y \neq 0$) for the original PDC [Fig. 5(e)] derives the anticrossing on the k_x axis [Fig. 5(f)] through the coupling between $|p_y\rangle$ and $|s\rangle$ of each band, leading to the band-gap opening. However, the x-directional symmetry breaking almost preserves the original PDC [Fig. 5(d)] due to the conservation of the orthogonality between $|p_y\rangle$ and $|s\rangle$ (or $|p_x\rangle$) (refer to Appendix C for derivation).

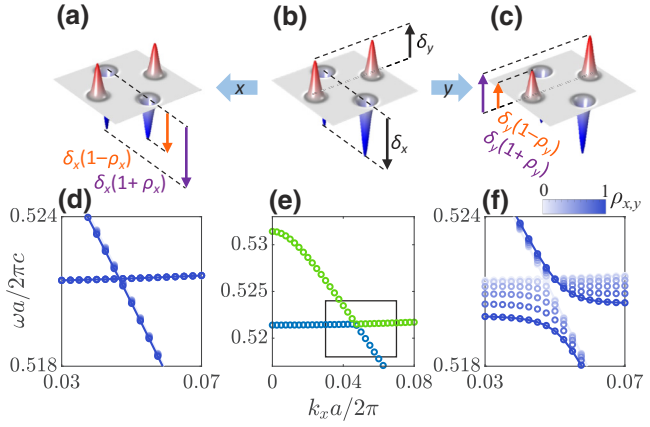

FIG. 5. (a)–(c) The profiles of mirror-symmetry-broken perturbations: (a),(c) perturbation functions $f(\mathbf{r})$ obtained with the asymmetry parameters ρ_x or ρ_y for the mirror symmetry breaking of (b) the original C_{2v}-symmetric perturbation function $f(\mathbf{r})$. (d)–(f) Corresponding dispersion relations of the lowest two bands for (a)–(c): (d),(f) the variations of the dispersion relations with gradual increases in $\rho_{x,y} \leq 1$, from (e) the dispersion relations for the perturbation point Q in Fig. 4(a). The rectangle in (e) shows the magnified range for (d),(f).

V. CONCLUSION

To summarize, we successfully design all types of tilted PDCs in a single platform of a square-lattice photonic crystal by developing a Hamiltonian-based analysis in view of the inversely designed spectral ordering. Specifically, we first classify the deformed band structures of the triply degenerate PDC and then verify the inverse-design method for the complete and deterministic design of optical structures. Through this process, the design of type-I, type-II, and type-III PDCs on the k_x axis is achieved by exploiting the nonzero slope of the flat band, achieving a tunable topological transition in k space. The effect of mirror symmetry breaking in relation to band-gap opening is also addressed for prospective applications. By extending our proposal to non-Hermitian systems of larger design freedom [34,35], we expect the realization of and transition between different types of Fermi arcs in a single platform. Likewise, by exploiting time-reversal symmetry breaking, our approach should be applicable to the design of a tilted PDC with extreme nonreciprocity at the Γ-point, which derives the unidirectional material phase transition around the zero index.

ACKNOWLEDGMENTS

We acknowledge financial support from the National Research Foundation of Korea (NRF) through the Global Frontier Program (2014M3A6B3063708) and the Basic Science Research Program (2016R1A6A3A04009723), all funded by the Korean government.

APPENDIX A: DERIVATION OF BAND ANTICROSSING NEAR A TYPE-III DIRAC POINT

The effective Hamiltonian for the deformation class D (without loss of generality, $\omega_s = \omega_{px} > \omega_{py}$) can be written using the Γ-point basis as the sum of on-axis Hamiltonian

for $k_y = 0$ and the other terms:

$$H(\mathbf{k}) = H_{\text{axis}} + V = \begin{bmatrix} \omega_s & v_x k_x & 0 \\ v_x k_x & \omega_s & 0 \\ 0 & 0 & \omega_{py} \end{bmatrix} + \begin{bmatrix} 0 & 0 & v_y k_y \\ 0 & 0 & 0 \\ v_y k_y & 0 & 0 \end{bmatrix}. \tag{A1}$$

The unperturbed Hamiltonian H_{axis} has three eigenfrequencies $\omega_{\pm}(k_x) = \omega_s \pm |v_x k_x|$ and $\omega_{\text{flat}}(k_x) = \omega_{py}$ with corresponding eigenmodes $|\pm\rangle = [1 \ \pm 1 \ 0]^T/\sqrt{2}$ and $|\text{flat}\rangle = [0 \ 0 \ 1]^T$, which form a single intersection point between the bands of ω_- and ω_{flat}, at $k_x = k_{x0} \equiv |(\omega_s - \omega_{py})/v_x|$.

For the perturbation with nonzero k_y, the first-order degenerate perturbation theory [33] derives the matrix elements of V with regard to $|-\rangle$ and $|\text{flat}\rangle$ as

$$\langle -|V|-\rangle = \frac{v_y k_y}{2} \begin{bmatrix} 1 & -1 & 0 \end{bmatrix} \begin{bmatrix} 0 & 0 & 1 \\ 0 & 0 & 0 \\ 1 & 0 & 0 \end{bmatrix} \begin{bmatrix} 1 \\ -1 \\ 0 \end{bmatrix} = 0 \tag{A2}$$

and $\langle \text{flat}|V|\text{flat}\rangle = 0$, $\langle -|V|\text{flat}\rangle = \langle \text{flat}|V|-\rangle = v_y k_y/\sqrt{2}$ in a similar way. Using the basis $\mathcal{W} = \{|-\rangle, |\text{flat}\rangle\}$, the perturbation is represented by

$$[V]_{\mathcal{W}} = \frac{v_y k_y}{\sqrt{2}} \begin{bmatrix} 0 & 1 \\ 1 & 0 \end{bmatrix}, \tag{A3}$$

which splits the degenerate frequency by new eigenvectors and corresponding eigenvalues: $\omega_\uparrow = v_y k_y/\sqrt{2}, \omega_\downarrow = -v_y k_y/\sqrt{2}$, $|\uparrow\rangle = (|-\rangle + |\text{flat}\rangle)/\sqrt{2}$, and $|\downarrow\rangle = (|-\rangle - |\text{flat}\rangle)/\sqrt{2}$. The band anticrossing near the DP is then given by $|\omega_\uparrow - \omega_\downarrow| = \sqrt{2}|v_y k_y|$, which originates from the coupling of the degenerate modes at the DP.

APPENDIX B: PERTURBATIVE INVERSE DESIGN METHOD

We employ a C_{2v}-symmetric multiplicative perturbation function $f_0(\mathbf{r})$ with parameters (δ_x, δ_y):

$$f_0(\mathbf{r}) = \delta_x \left[\phi\left(\frac{x-d}{\sigma}, \frac{y}{\sigma}\right) + \phi\left(\frac{x+d}{\sigma}, \frac{y}{\sigma}\right) \right] + \delta_y \left[\phi\left(\frac{x}{\sigma}, \frac{y-d}{\sigma}\right) + \phi\left(\frac{x}{\sigma}, \frac{y+d}{\sigma}\right) \right], \tag{B1}$$

where $d = a/3$, $\sigma = 0.035a$, and $\phi(\xi, \eta) = e^{-(\xi^2+\eta^2)/2}$. Because our design is restricted in the finite unit cell $\mathbf{r} \in [-a/2, a/2]^2$ with periodic boundary conditions, we use a differentiable form at the boundary ($\partial f/\partial \mathbf{n} \sim 0$) by symmetrizing for the boundary:

$$f(\mathbf{r}) = \sum_{\mathbf{R}} f_0(\mathbf{r} - \mathbf{R}), \tag{B2}$$

where $\mathbf{R} = a(n_x, n_y)$ represents a few lattice vectors for integers $n_{x,y} = 0$ or ± 1.

APPENDIX C: EFFECT OF MIRROR SYMMETRY BREAKING

In this appendix, we examine quantitatively the effect of mirror-asymmetric function. For example, broken mirror symmetry in the y direction can be achieved by rewriting the perturbation function in Eq. (B1) as

$$f_0(\mathbf{r}) = \delta_x \left[\phi\left(\frac{x-d}{\sigma}, \frac{y}{\sigma}\right) + \phi\left(\frac{x+d}{\sigma}, \frac{y}{\sigma}\right) \right] + \delta_y (1+\rho_y) \phi\left(\frac{x}{\sigma}, \frac{y-d}{\sigma}\right) + \delta_y (1-\rho_y) \phi\left(\frac{x}{\sigma}, \frac{y+d}{\sigma}\right) \tag{C1}$$

with nonzero asymmetry parameter ρ_y. This modifies the on-axis Hamiltonian in Eq. (A1) to

$$H_{\text{axis}} = H^{(0)}_{\text{axis}} + V_y = \left[H^{(0)}_{\text{axis}} + V_y^{(+)}\right] + V_y^{(-)} = H'_{\text{axis}} + V_y^{(-)}, \tag{C2}$$

where

$$H^{(0)}_{\text{axis}} = \begin{bmatrix} \omega_s^{(0)} & v_x^{(0)} k_x & 0 \\ v_x^{(0)} k_x & \omega_{px}^{(0)} & 0 \\ 0 & 0 & \omega_{py}^{(0)} \end{bmatrix} \tag{C3}$$

is the k_x-axis Hamiltonian when $\rho_y = 0$, V_y is the perturbation by turning on the parameter ρ_y, $V_y^{(\pm)} = (V_y \pm P_y V_y P_y)/2$ are the even $(+)$ and the odd $(-)$ part of V_y with respect to y-inversion operator P_y, satisfying $V_y^{(\pm)} P_y = \pm P_y V_y^{(\pm)}$, and

$$H'_{\text{axis}} = \begin{bmatrix} \omega_s & v_x k_x & 0 \\ v_x k_x & \omega_{px} & 0 \\ 0 & 0 & \omega_{py} \end{bmatrix} \tag{C4}$$

is a new k_x-axis Hamiltonian in which the even part of perturbation $V_y^{(+)}$ is taken into account for a new set of Γ-point eigenfrequencies (ω_s, ω_{px}, and ω_{py}) and velocity coefficients (v_x, v_y). It is noted that the nonzero ρ_y cannot ensure that the perturbation is fully odd; however, the even part $V_y^{(+)}$ does not change the symmetric properties significantly because it is still C_{2v}-symmetric due to even parity in x direction as well as y direction.

The perturbation by the odd part $V_y^{(-)}$ is applied to the DP on the k_x axis, which is defined by the new Hamiltonian H'_{axis}. Without loss of generality, the DP is made up of two degenerate states $|-\rangle = c_s\,|s\rangle + c_{px}\,|p_x\rangle$ and $|\text{flat}\rangle = |p_y\rangle$ with arbitrary coefficients c_s and c_{px}. From symmetry considerations of $V_y^{(-)}$ such that $V_y^{(-)}(x,y) = +V_y^{(-)}(-x,y) = -V_y^{(-)}(x,-y)$ in the position-space representation, we obtain the following matrix elements:

$$\langle -|V_y^{(-)}|\text{flat}\rangle = c_s^*\langle s|V_y^{(-)}|\text{flat}\rangle \neq 0 \tag{C5}$$

due to the fact that

$$\int_{-a/2}^{a/2} u_{px}^* V_y^{(-)} u_{py}\,dx = 0, \quad \int_{-a/2}^{a/2} u_s^* V_y^{(-)} u_{py}\,dx(dy) \neq 0, \tag{C6}$$

while $\langle -|V_y^{(-)}|-\rangle = \langle \text{flat}|V_y^{(-)}|\text{flat}\rangle = 0$. The nonzero off-diagonal matrix element $\langle -|V_y^{(-)}|\text{flat}\rangle$ thus means the band anticrossing even on the axis.

On the other hand, the Hamiltonian with broken x mirror symmetry is written as

$$H_{\text{axis}} = H_{\text{axis}}^{(0)} + V_x = \left[H_{\text{axis}}^{(0)} + V_x^{(+)}\right] + V_x^{(-)} = H'_{\text{axis}} + V_x^{(-)} \tag{C7}$$

for a modified perturbation function with nonzero ρ_x:

$$\begin{aligned} f_0(\mathbf{r}) = {} & \delta_y\left[\phi\left(\frac{x}{\sigma},\frac{y-d}{\sigma}\right) + \phi\left(\frac{x}{\sigma},\frac{y+d}{\sigma}\right)\right] \\ & + \delta_x(1+\rho_x)\phi\left(\frac{x-d}{\sigma},\frac{y}{\sigma}\right) \\ & + \delta_x(1-\rho_x)\phi\left(\frac{x+d}{\sigma},\frac{y}{\sigma}\right). \end{aligned} \tag{C8}$$

In this case, the matrix elements are determined by

$$\langle -|V_x^{(-)}|-\rangle = 2\,\text{Re}\,\langle s|V_x^{(-)}|p_x\rangle, \tag{C9}$$

which is not necessarily zero, and $\langle \text{flat}|V_x^{(-)}|\text{flat}\rangle = \langle \text{flat}|V_x^{(-)}|-\rangle = 0$ from similar symmetry considerations with Eq. (C6). There is a significant difference from the previous case of y mirror symmetry breaking; the possibly nonzero matrix element in Eq. (C9) is at the diagonal position, which just shifts the band ω_- but does not lead to the coupling between the two bands. Therefore, they still maintain the "crossing" state. The FEM calculations in Figs. 5(d) and 5(f) verify this result.

[1] K. S. Novoselov, A. K. Geim, S. V. Morozov, D. Jiang, M. I. Katsnelson, I. V. Grigorieva, S. V. Dubonos, and A. A. Firsov, Two-dimensional gas of massless Dirac fermions in graphene, Nature **438**, 197 (2005).

[2] J.-H. Chen, C. Jang, S. Xiao, M. Ishigami, and M. S. Fuhrer, Intrinsic and extrinsic performance limits of graphene devices on SiO2, Nat. Nanotechnol. **3**, 206 (2008).

[3] K. Bolotin, K. Sikes, Z. Jiang, M. Klima, G. Fudenberg, J. Hone, P. Kim, and H. Stormer, Ultrahigh electron mobility in suspended graphene, Solid State Commun. **146**, 351 (2008).

[4] N. Tombros, C. Jozsa, M. Popinciuc, H. T. Jonkman, and B. J. van Wees, Electronic spin transport and spin precession in single graphene layers at room temperature, Nature **448**, 571 (2007).

[5] B. Dlubak, M.-B. Martin, C. Deranlot, B. Servet, S. Xavier, R. Mattana, M. Sprinkle, C. Berger, W. A. D. Heer, F. Petroff, A. Anane, P. Seneor, and A. Fert, Highly efficient spin transport in epitaxial graphene on SiC, Nat. Phys. **8**, 557 (2012).

[6] O. Peleg, G. Bartal, B. Freedman, O. Manela, M. Segev, and D. N. Christodoulides, Conical Diffraction and Gap Solitons in Honeycomb Photonic Lattices, Phys. Rev. Lett. **98**, 103901 (2007).

[7] X. Huang, Y. Lai, Z. H. Hang, H. Zheng, and C. T. Chan, Dirac cones induced by accidental degeneracy in photonic crystals and zero-refractive-index materials, Nat. Mater. **10**, 582 (2011).

[8] P. Moitra, Y. Yang, Z. Anderson, I. I. Kravchenko, D. P. Briggs, and J. Valentine, Realization of an all-dielectric zero-index optical metamaterial, Nat. Photonics **7**, 791 (2013).

[9] J.-W. Dong, M.-L. Chang, X.-Q. Huang, Z. H. Hang, Z.-C. Zhong, W.-J. Chen, Z.-Y. Huang, and C. T. Chan, Conical Dispersion and Effective Zero Refractive Index in Photonic Quasicrystals, Phys. Rev. Lett. **114**, 163901 (2015).

[10] J. Mei, Y. Wu, C. T. Chan, and Z.-Q. Zhang, First-principles study of Dirac and Dirac-like cones in phononic and photonic crystals, Phys. Rev. B **86**, 035141 (2012).

[11] J. Lu, C. Qiu, S. Xu, Y. Ye, M. Ke, and Z. Liu, Dirac cones in two-dimensional artificial crystals for classical waves, Phys. Rev. B **89**, 134302 (2014).

[12] J. Ningyuan, C. Owens, A. Sommer, D. Schuster, and J. Simon, Time- and Site-Resolved Dynamics in a Topological Circuit, Phys. Rev. X **5**, 021031 (2015).

[13] W. Zhu, S. Hou, Y. Long, H. Chen, and J. Ren, Simulating quantum spin Hall effect in the topological Lieb lattice of a linear circuit network, Phys. Rev. B **97**, 075310 (2018).

[14] F. D. M. Haldane, Model for a Quantum Hall Effect Without Landau Levels: Condensed-Matter Realization of the "Parity Anomaly", Phys. Rev. Lett. **61**, 2015 (1988).

[15] M. C. Rechtsman, J. M. Zeuner, A. Tünnermann, S. Nolte, M. Segev, and A. Szameit, Strain-induced pseudomagnetic field and photonic landau levels in dielectric structures, Nat. Photon. **7**, 153 (2012).

[16] L.-H. Wu and X. Hu, Scheme for Achieving a Topological Photonic Crystal by Using Dielectric Material, Phys. Rev. Lett. **114**, 223901 (2015).

[17] J. Mei, Z. Chen, and Y. Wu, Pseudo-time-reversal symmetry and topological edge states in two-dimensional acoustic crystals, Sci. Rep. **6**, 32752 (2016).

[18] X. Wen, C. Qiu, Y. Qi, L. Ye, M. Ke, F. Zhang, and Z. Liu, Acoustic landau quantization and quantum-hall-like edge states, Nat. Phys. **15**, 352 (2019).

[19] A. A. Soluyanov, D. Gresch, Z. Wang, Q. Wu, M. Troyer, X. Dai, and B. A. Bernevig, Type-II Weyl semimetals, Nature **527**, 495 (2015).

[20] M. Milićević, G. Montambaux, T. Ozawa, O. Jamadi, B. Real, I. Sagnes, A. Lemaître, L. Le Gratiet, A. Harouri, J. Bloch, and A. Amo, Type-III and Tilted Dirac Cones Emerging From Flat Bands in Photonic Orbital Graphene, Phys. Rev. X **9**, 031010 (2019).

[21] T. Kawarabayashi, Y. Hatsugai, T. Morimoto, and H. Aoki, Generalized chiral symmetry and stability of zero modes for tilted dirac cones, Phys. Rev. B **83**, 153414 (2011).

[22] M. Trescher, B. Sbierski, P. W. Brouwer, and E. J. Bergholtz, Quantum transport in dirac materials: Signatures of tilted and anisotropic dirac and weyl cones, Phys. Rev. B **91**, 115135 (2015).

[23] Y. D. Chong, X.-G. Wen, and M. Soljačić, Effective theory of quadratic degeneracies, Phys. Rev. B **77**, 235125 (2008).

[24] W.-Y. He and C. T. Chan, The emergence of dirac points in photonic crystals with mirror symmetry, Sci. Rep. **5**, 8186 (2015).

[25] H. Huang, S. Zhou, and W. Duan, Type-II Dirac fermions in the $PtSe_2$ class of transition metal dichalcogenides, Phys. Rev. B **94**, 121117(R) (2016).

[26] G. G. Pyrialakos, N. S. Nye, N. V. Kantartzis, and D. N. Christodoulides, Emergence of Type-II Dirac Points in Graphynelike Photonic Lattices, Phys. Rev. Lett. **119**, 113901 (2017).

[27] H.-X. Wang, Y. Chen, Z. H. Hang, H.-Y. Kee, and J.-H. Jiang, Type-II dirac photons, npj Quantum Mater. **2**, 54 (2017).

[28] J. Y. Lin, N. C. Hu, Y. J. Chen, C. H. Lee, and X. Zhang, Line nodes, Dirac points, and Lifshitz transition in two-dimensional nonsymmorphic photonic crystals, Phys. Rev. B **96**, 075438 (2017).

[29] C. Hu, Z. Li, R. Tong, X. Wu, Z. Xia, L. Wang, S. Li, Y. Huang, S. Wang, B. Hou, C. T. Chan, and W. Wen, Type-II Dirac Photons at Metasurfaces, Phys. Rev. Lett. **121**, 024301 (2018).

[30] Z. Yang and B. Zhang, Acoustic Type-II Weyl Nodes From Stacking Dimerized Chains, Phys. Rev. Lett. **117**, 224301 (2016).

[31] X. Wu, X. Li, R.-Y. Zhang, X. Xiang, J. Tian, Y. Huang, S. Wang, B. Hou, C. T. Chan, and W. Wen, Deterministic Scheme for Two-Dimensional Type-II Dirac Points and Experimental Realization in Acoustics, Phys. Rev. Lett. **124**, 075501 (2020).

[32] B. Xie, H. Liu, H. Cheng, Z. Liu, S. Chen, and J. Tian, Experimental Realization of Type-II Weyl Points and Fermi Arcs in Phononic Crystal, Phys. Rev. Lett. **122**, 104302 (2019).

[33] M. S. Dresselhaus, G. Dresselhaus, and A. Jorio, *Group Theory: Application to the Physics of Condensed Matter* (Springer, New York, NY, 2008).

[34] B. Zhen, C. W. Hsu, Y. Igarashi, L. Lu, I. Kaminer, A. Pick, S.-L. Chua, J. D. Joannopoulos, and M. Soljačić, Spawning rings of exceptional points out of Dirac cones, Nature **525**, 354 (2015).

[35] H. Zhou, C. Peng, Y. Yoon, C. W. Hsu, K. A. Nelson, L. Fu, J. D. Joannopoulos, M. Soljačić, and B. Zhen, Observation of bulk Fermi arc and polarization half charge from paired exceptional points, Science **359**, 1009 (2018).

[36] J. D. Joannopoulos, S. G. Johnson, J. N. Winn, and R. D. Meade, *Photonic Crystals: Molding the Flow of Light* (Princeton University Press, Princeton, NJ, 2008), 2nd ed.

[37] X.-T. He, Y.-N. Zhong, Y. Zhou, Z.-C. Zhong, and J.-W. Dong, Dirac directional emission in anisotropic zero refractive index photonic crystals, Sci. Rep. **5**, 13085 (2015).

[38] D. R. Smith, S. Schultz, P. Markoš, and C. M. Soukoulis, Determination of effective permittivity and permeability of metamaterials from reflection and transmission coefficients, Phys. Rev. B **65**, 195104 (2002).

[39] See Supplemental Material at http://link.aps.org/supplemental/10.1103/PhysRevApplied.13.044015 for the effective wave parameter analysis, the dipole-based design, and the practical implementation with the flat band control.

[40] S. Yu, X. Piao, J. Hong, and N. Park, Metadisorder for designer light in random systems, Sci. Adv. **2**, e1501851 (2016).

[41] S. Yu, X. Piao, and N. Park, Bohmian Photonics for Independent Control of the Phase and Amplitude of Waves, Phys. Rev. Lett. **120**, 193902 (2018).

[42] X. Piao, S. Yu, and N. Park, Design of Transverse Spinning of Light with Globally Unique Handedness, Phys. Rev. Lett. **120**, 203901 (2018).

[43] COMSOL Multiphysics v5.3.

[44] D. P. Bertsekas, *Nonlinear Programming* (Athena Scientific, Nashua, NH, 2016), 3rd ed.

[45] H. N. S. Krishnamoorthy, Z. Jacob, E. Narimanov, I. Kretzschmar, and V. M. Menon, Topological transitions in metamaterials, Science **336**, 205 (2012).

[46] J. S. Gomez-Diaz, M. Tymchenko, and A. Alù, Hyperbolic Plasmons and Topological Transitions Over Uniaxial Metasurfaces, Phys. Rev. Lett. **114**, 233901 (2015).

[47] D. Xiao, W. Yao, and Q. Niu, Valley-Contrasting Physics in Graphene: Magnetic Moment and Topological Transport, Phys. Rev. Lett. **99**, 236809 (2007).

[48] T. Ma and G. Shvets, All-Si valley-hall photonic topological insulator, New J. Phys. **18**, 025012 (2016).

[49] J. B. Oostinga, H. B. Heersche, X. Liu, A. F. Morpurgo, and L. M. K. Vandersypen, Gate-induced insulating state in bilayer graphene devices, Nat. Mater. **7**, 151 (2007).

[50] J. P. Dowling, M. Scalora, M. J. Bloemer, and C. M. Bowden, The photonic band edge laser: A new approach to gain enhancement, J. Appl. Phys. **75**, 1896 (1994).